Interferometric measurement of back focal length and insertion loss of precision microlens arrays

Phillip H. Malyak[*a], David L. Kent*[a], Paul Kolodner**[b] , John Crawford*[a]
[a]Zygo TeraOptix; [b]Bell Laboratories, Lucent Technologies

ABSTRACT

Microlenses are being applied widely, especially in fiber-optic components and modules. The lenses are frequently made in arrays which are coupled with fiber arrays to make arrays of collimated laser beams. A back focal length (BFL) that is uniform across the array and a low average insertion loss are critical for many applications. In this paper, we describe interferometric techniques for measuring the BFL and IL of all elements in a microlens array, and we document the measurement precision.

The BFL of a lens can be measured interferometrically by illuminating it with a point source that is generated by a converging lens in the test leg of the interferometer. The point source is initially located at the back focal point of the lens under test (i.e., confocal configuration) and a plane mirror reflects the beam back through the lens and into the interferometer. The interferometer is then moved axially to obtain the cat's-eye reflection from the back surface of the lens. The BFL is equal to the axial distance between these two points. We report results of measurements of BFL and IL of microlenses having nominal BFL of 3.4 mm. The BFL is measured to a precision of <4 μm. The precision depends primarily on the test wavelength and the n.a. of the test part, and these relationships are described. The IL is a function of transmitted wavefront error, and we compare wavefront-derived IL to the directly-measured IL.

Keywords: optical testing, interferometry, microlenses, microoptics

1. INTRODUCTION

Many fiberoptic packages use microoptic components or devices (e.g., lenses, switches, filters, gratings, etc.) as illustrated in Figure 1a. The fundamental building blocks of such a package consists of 4 elements: an input fiber, a pair of air-spaced collimating lenses and an output fiber. Arrayed packages can be built by using fiber arrays and lens arrays as shown in Figure 1b. Additional microoptic components are located between the collimating lenses as shown. Optical coupling through the package must usually be performed in a relatively loss-free manner. In order for the package configuration in Figure 1 to have low loss, the optical elements between the input and output fibers must produce a field distribution on the output fiber that matches the mode-field of the output fiber. A number of factors can contribute to insertion loss (e.g., scatter, Fresnel reflection, alignment errors and fabrication errors). The purpose of this paper is to consider losses due to fabrication errors; i.e., the errors that cause the optics to form an aberrated spot on the output fiber. Specifically, we consider two classes of aberrations (1) variations in lens focal length and (2) higher order aberrations. The aberrations are measured interferometrically, and their effect on insertion loss is presented.

A variation in focal length from lens-to-lens in an arrayed package will result in an insertion loss that cannot be easily compensated. The inability to simply refocus is prohibited by the physical constraints of working with monolithic fiber arrays and lens arrays. The measurement of focal length is described in Sections 2 and 3. In particular, interferometric measurement of focal length is described, the theoretical precision of the measurement is presented and experimental results are given. Differences between the physical- and geometrical-optics phenomena are described.

The measurement of higher-order aberrations and the resulting effect on IL is described in Section 4. In particular, the wavefront distortion of lenses is measured interferometrically and IL is computed from the measured wavefront error. The IL is also measured directly and the correlation between the direct versus interferometric measurement is presented.

---

* pmalyak@zygoteraoptix.com; phone 1 508 429-5696; fax 1 508 429-2071; http://www.zygoteraoptix.com; Zygo TeraOptix, 100 Kuniholm Drive, Holliston, MA, USA, 01746; ** prk@lucent.com; phone 1 908 582-7021; fax 1 908 582-4702; http://www.lucent.com; Room 1E-314 Bell Laboratories, 600 Mountain Avenue, Murray Hill, NJ, USA 07974-0636

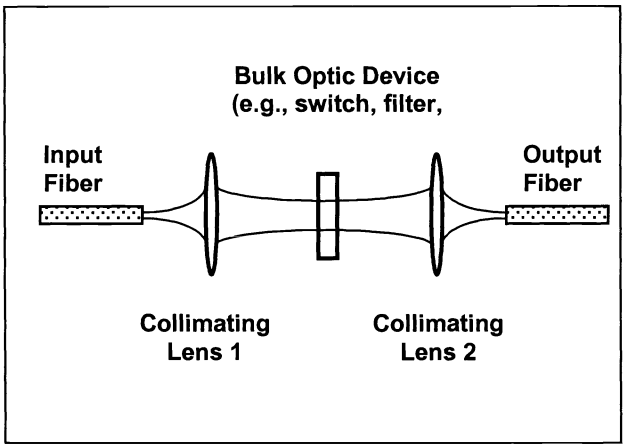

Figure 1a: Schematic of fiberoptic package.

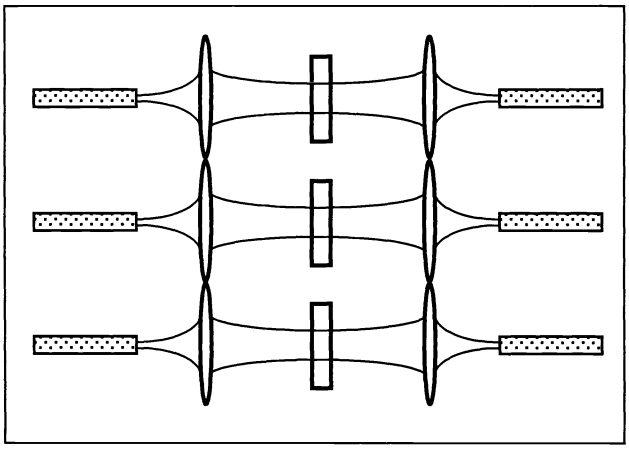

Figure 1b: 1 x 3 arrayed package using monolithic fiber and lens arrays.

2. INTERFEROMETER CONFIGURATION

The instrument used to characterize the microlenses is a phase-shifting Twyman-Green interferometer which is illustrated schematically in Figure 2. A photograph of the instrument is shown in Figure 3. It is a commercially available interferometer (MicroLUPI[1]) that normally operates at $\lambda = 0.633$ μm, but has been modified to work at $\lambda = 1.55$ μm. The lens under test, L1, is placed in the confocal position (Position 1) in order to test the lens at infinite conjugates. A flat mirror is placed in the collimated space below L1 to perform a double pass test. L1 is then moved to Position 2 (i.e., the focal point of the converging lens) to obtain a cat's-eye retro-reflection from the apex of the back surface. The back focal length is determined by using a precision encoder to measure the distance between Positions 1 and 2. A small error results when measuring either Position 1 or 2 if the test leg of the interferometer is not completely nulled. Since the interferometer measures the residual power in the wavefront at both positions, this error may be quantified and a correction term can then be applied to correct for the error.[2] Calculating the correction term is described in Section 3.1.

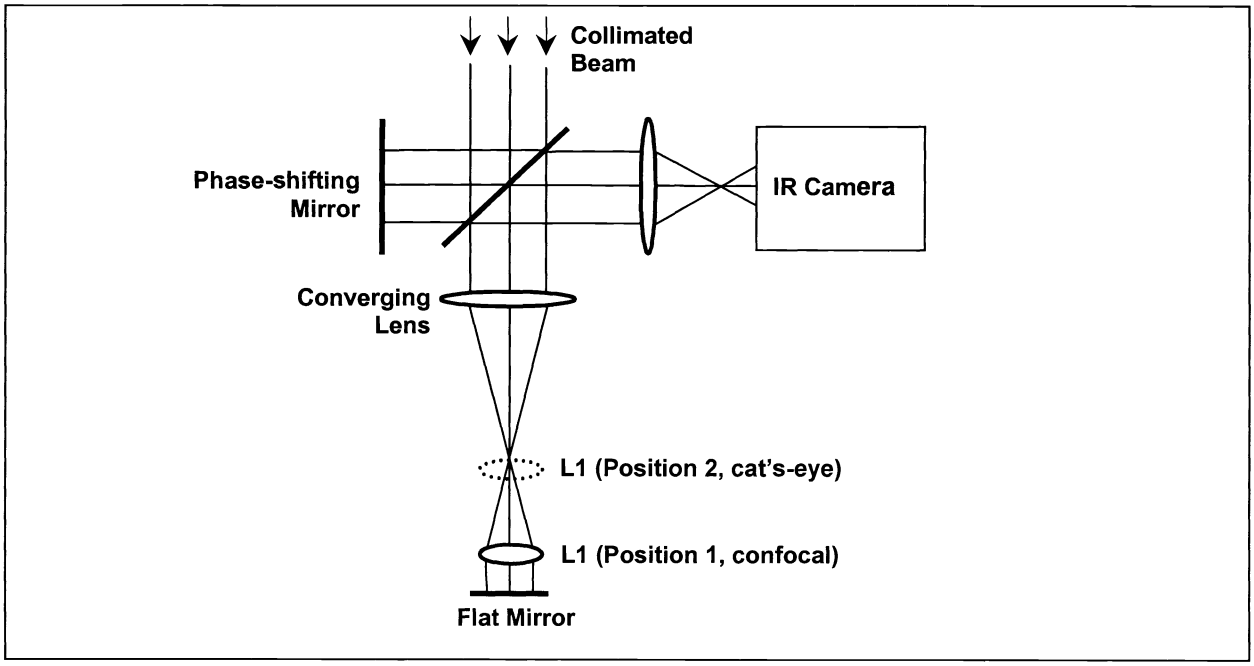

Figure 2: Phase-shifting Twyman-Green interferometer.

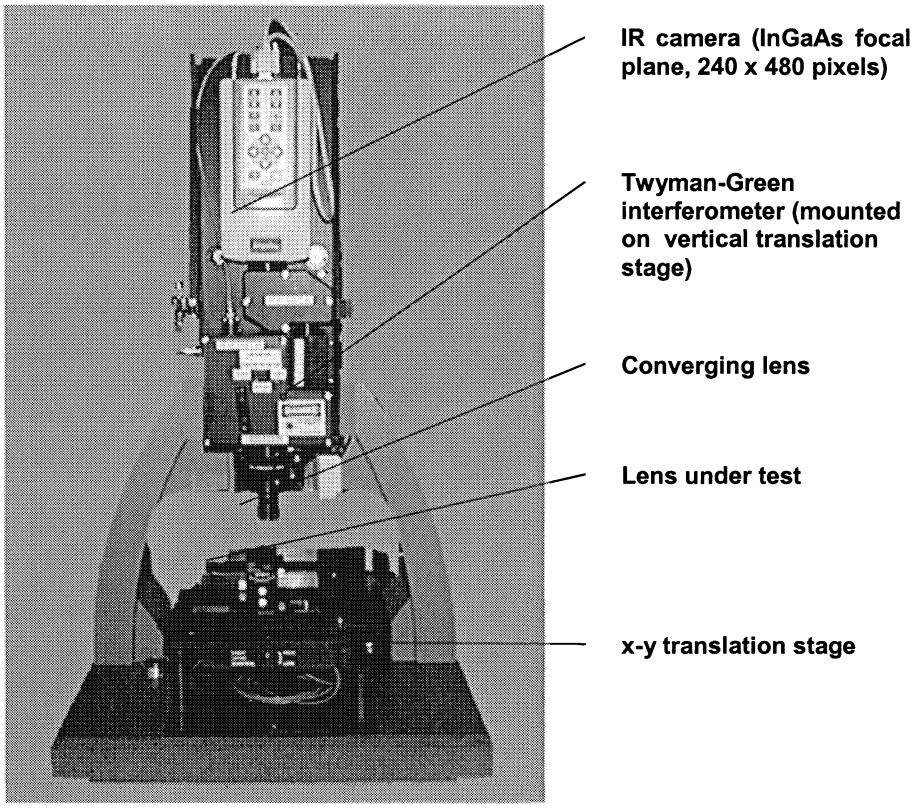

Figure 3: Photograph of the IR interferometer used for measuring microlenses (at $\lambda = 1.55$ μm). The interferometer is mounted vertically on a motorized translation stage (z-axis). The test beam is pointing down. The lens under test is mounted on a motorized x-y translation stage. The stages operate under computer control to permit automated testing.

3. MEASUREMENT OF BACK FOCAL LENGTH

The back focal length of the lens is measured interferometrically as shown in Figure 2 (and described above). Although the interferometric measurement is inherently a physical optics phenomenon, it is adequately described by geometrical optics for modeling purposes. In Section 3.1, we describe the interferometric measurement and its precision. In Section 3.2, we show that a physical-optics model is required to describe the beam propagation within the package. Results obtained from the physical-optics model are compared to experimental data, confirming that physical-optics behavior is dominant.

3.1 Interferometer calibration and measurement precision

The precision with which the focal point of the lens can be determined is directly related to the precision with which the interferometer can measure a change in curvature of an incident wavefront. Thus, the relationship between these two parameters must be considered. In particular, the separation Δz between the centers of curvature of two spherical surfaces with different radii of curvature is given by the following expression [3]:

$$\delta = (1 - \cos\theta)\,\Delta z \quad , \tag{1}$$

where the symbols in the above equation are defined in Figure 4. Using the small angle approximation and setting the numerical aperture, *n.a.*, equal to θ yields

$$\Delta z = \frac{\delta}{1 - \sqrt{1 - \sin^2\theta}} \approx \frac{2\delta}{(n.a.)^2} \quad . \tag{2}$$

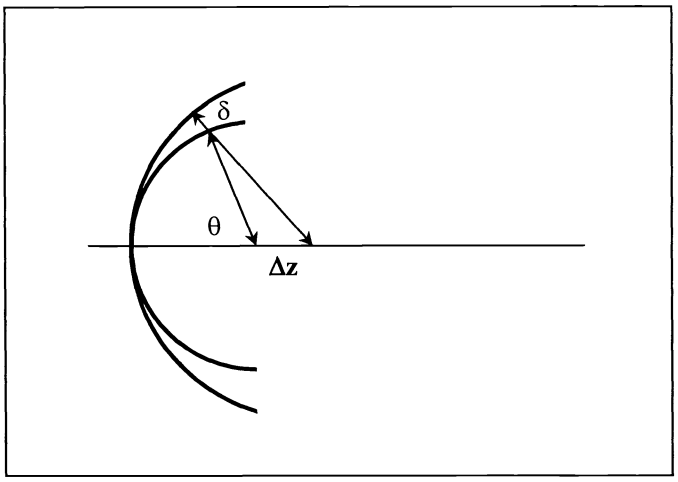

Figure 4: Geometry showing the separation between the centers of curvature of two spheres with different radii.

An axial calibration was performed by using a concave reference mirror in the test leg of the interferometer and moving it along the z-axis in known increments. At each increment, the power of the wavefront (i.e., one-half the peak-to-valley value of the best-fit paraboloid) is measured and plotted. A typical plot of power vs. axial position is shown in Figure 5, which also show the best-fit straight line to the experimental data. The slope of this line is 0.0030 waves per μm; this represents the axial calibration constant of the instrument. The data were taken with the interferometer operating at $\lambda = 1.55$ μm and *n.a.* = .095. The theoretical value of the axial calibration may be determined by substituting the above values for λ and *n.a.* into Equation (2):

$$\delta_{1/2} / \Delta z_{mirror} = .0029 \quad \lambda / \mu m \ , \tag{3}$$

where $\Delta z = 2\Delta z_{mirror}$ and $\delta_{1/2} = \delta/2$; and i.e., the focal spot produced by the reference mirror is displaced by twice the physical motion of the reference mirror. Thus, the measured calibration constant of the interferometer closely agrees with the theoretical value. The calibration constant is used to determine the correction term that needs to be applied if the interferometer is not completely nulled. In particular, the residual power in waves at either Position 1 or 2 is divided by the calibration constant to give the correction in microns.

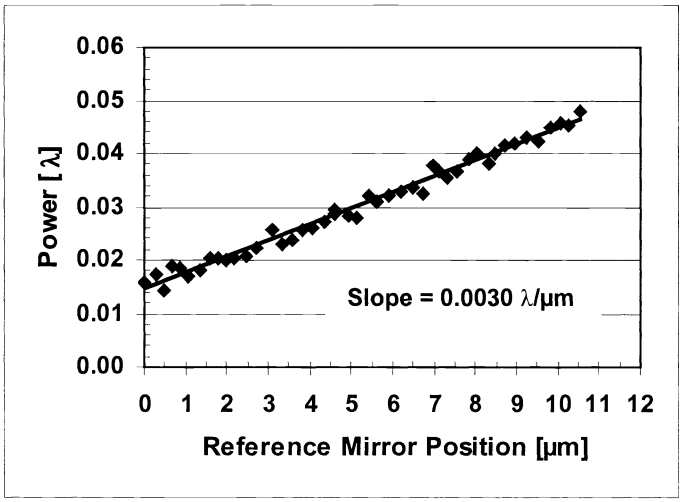

Figure 5: Plot of measured power vs reference mirror position. The slope of the best-fit straight line represents the axial calibration constant of the interferometer.

The results of 25 measurements of the BFL of a single silicon microlens are summarized in the histogram in Figure 6. The measurements are made at $\lambda = 1.55$ μm and *n.a.* = 0.133; the nominal focal length of the lens is 3.46 mm and the clear aperture is 1 mm in diameter. The plot in Figure 5 indicates that a change in power of 0.01λ is readily measured by the interferometer. Therefore, Equation (2) indicates that the measurement precision of the BFL of L1 should be ~1.8 μm. The data in Figure 6 indicate a measurement precision of 2 μm (1 standard deviation), which closely agrees with the predicted value. It should be noted that the residual error is quite small: 2 μm represents an error of 0.06% relative to the mean BFL.

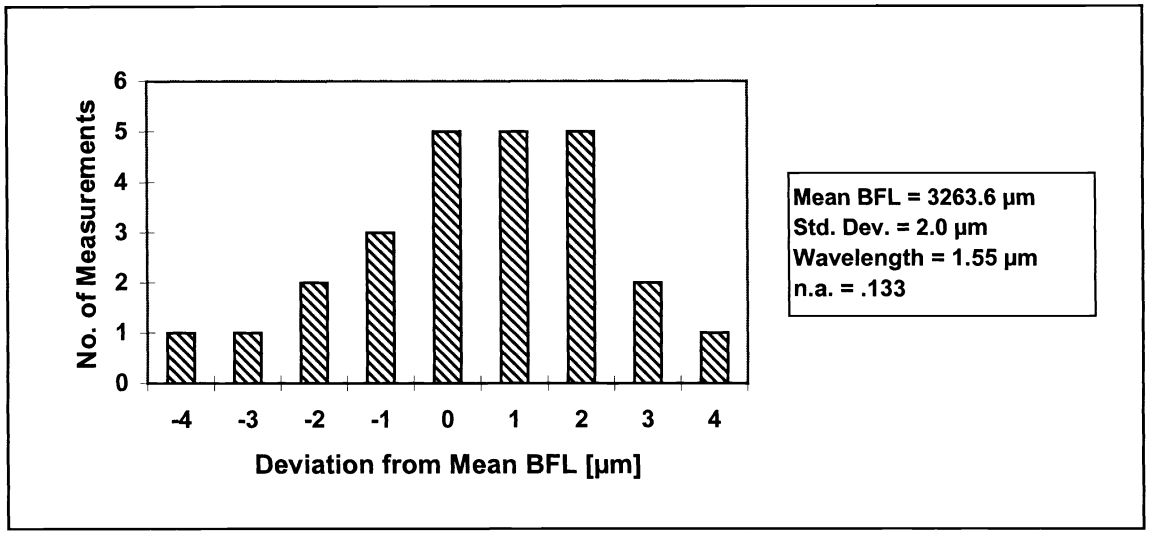

Figure 6: Histogram of 25 measurements of the BFL of a silicon microlens. The data indicate that the interferometric measurement is highly repeatable.

3.2 Back focal length and Gaussian beam propagation

Prior to using interferometry, our original tests of the microlenses were done in a manner that directly simulates the conditions of actual use. The experimental layout used for the direct measurement is shown in Figure 7; it is essentially one-half of the layout shown in Figure 1a. with a flat mirror place half-way between the two collimating lenses. The mirror is located at the nominal waist position of the Gaussian beam. The fiber can be moved along three translation axes to maximize the intensity at the detector. The axial distance between the lens and fiber is related to the BFL of the lens (but is not equal to the BFL) because physical optics phenomena become significant as a result of the Gaussian beam illumination provided by the fiber.

A comparison of results obtained by the direct method and the interferometric method is shown in Figure 8. The plot shows IL vs. lens to fiber distance. One curve shows the directly measured data, while the other shows the calculated IL based on an optical model of the system. The optical model uses the nominal lens prescription appropriately scaled to match the measured BFL of the lens under test. The lens is a plano-convex asphere and its prescription is summarized in Table 1. The optical modeling was done with OSLO[4] by tracing a paraxial Gaussian beam through the system and computing the coupling efficiency of the light that returns to the fiber. The model does not account for aberrations; as a result, the calculated IL becomes zero when the field distribution of the return beam matches the fundamental mode of the fiber. The directly measured data show a curve that is similar in shape to the calculated curve; however, the minimum IL is approximately 0.6 dB. The minimum IL from the direct data occurs at z = 2756 μm, while the interferometer gives a BFL of 2711 μm. The likely cause of the discrepancy is residual aberration in the lens that is not accounted for in the paraxial model.

Both curves in Figure 8 exhibit the same general shape; i.e., a relatively broad minimum followed by a rapid increase in IL to either side of the minimum. The differences include the minimum IL of 0.6 dB mentioned above as well as the width of the minimum region; in particular, the minimum of the calculated IL curve is wider than the measured curve. The differences are probably due to the residual aberration of the lens (primarily spherical aberration) which is not accounted for in the model.

An interesting feature revealed by the model is that, within the broad minimum, a beam waist occurs at 3 different axial locations (2.760, 2.766 and 2.772 mm). This is illustrated by the plots in Figures 9 – 11. Figure 9 shows the calculated spot diameter at the fiber as a function of lens-fiber spacing, while Figures 10 and 11 show the wavefront curvature of the Gaussian beam at the fiber. As expected, the waist radius is nearly constant over the region of minimum IL and the wavefront curvature is small. The presence of 3 waists is evident from Figure 11, which shows 3 distinct zeros in the wavefront curvature.

Surface No.	Radius [mm]	Thickness [mm]	Refractive Index	Conic Constant	Aperture Diam [mm]
1	2.6125	1.000	1.800	-0.68824	1.00
2	∞	-	1.000	-	1.00

Table 1: Optical prescription of lens used to produce the calculated IL curve in Figure 8.

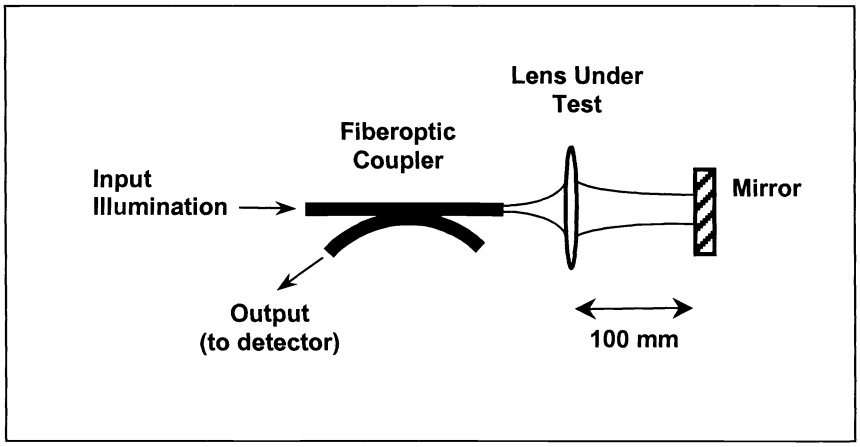

Figure 7: Experimental setup for direct measurement of microlens performance. The fiber is translated along 3 axis until maximum signal is observed. The axial distance between lens and fiber is related to the BFL of the lens.

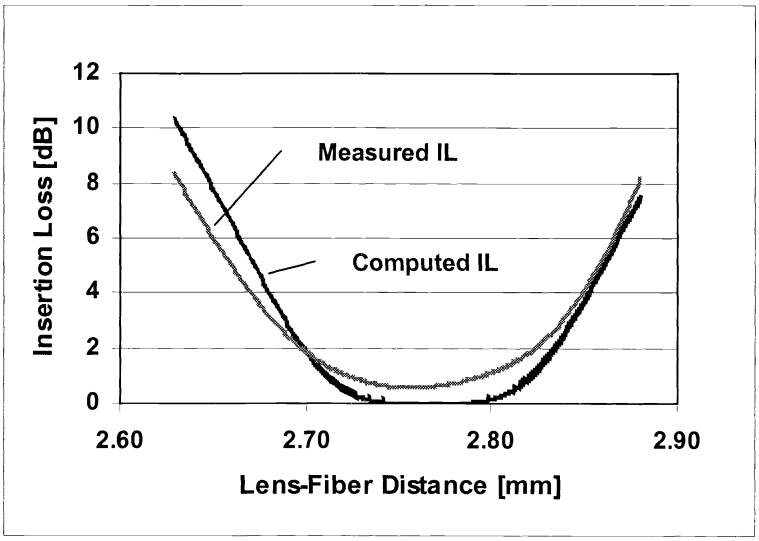

Figure 8: Plots of measured and computed IL as a function of lens-fiber distance for the lens described in Table 1. The BFL of the lens was measured interferometrically as 2711 mm; the direct measurement indicates that the minimum IL occurs at 2756 mm.

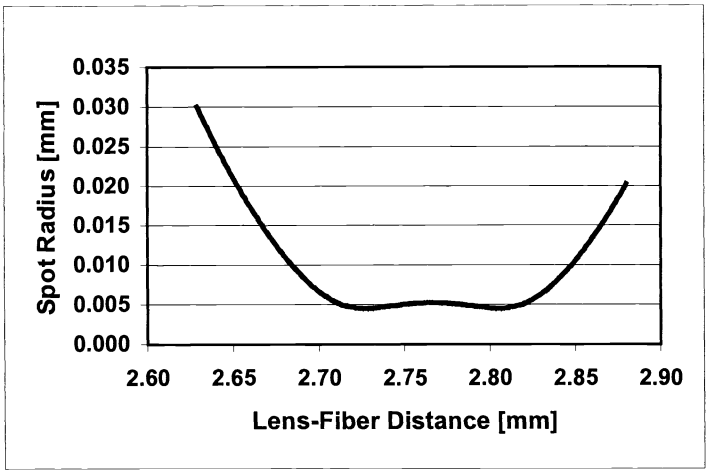

Figure 9: Plot of the calculated spot radius as a function of lens-fiber distance. The spot radius closely matches the mode-field radius of the fiber (5.2 μm) for $2.72 < z < 2.82$ mm.

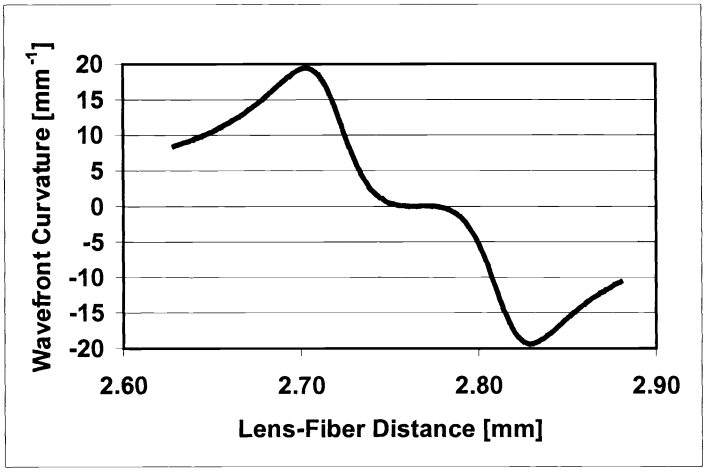

Figure 10: Plot of the calculated wavefront curvature as a function of lens-fiber distance. The wavefront is nearly planar (i.e., the curvature is nearly 0) near $z = 2.76$ μm.

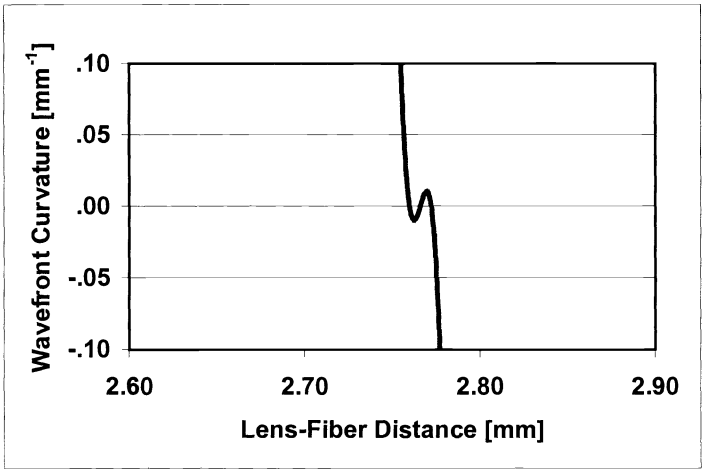

Figure 11: Same as above, except the vertical scale is expanded to show the points where curvature = 0 (2.760, 2.766 and 2.772 mm).

4. WAVEFRONT ABERRATION AND INSERTION LOSS.

We would expect random wavefront aberrations to yield a quadratic relationship between rms wavefront error and insertion loss.[5] However, as shown in Figure 12, this relationship did not hold for the sample of lenses that we examined. Loss does indeed increase with increasing wavefront error, but the spread of the data is of the order of 2 dB for moderate loss which is too large for our purposes. This spread is due in part to a large number of lenses which appear to exhibit high wavefront error but low insertion loss. Apparently, there is a component of aberration which does not strongly contribute to insertion loss. And, in fact, it turns out that these high-aberration, low-loss lenses exhibit excess astigmatism. This observation suggests that an appropriate method for analyzing the data is to do a multilinear fit of insertion loss to the Seidel aberration coefficients for astigmatism, coma and spherical aberration, to account for the fact that they contribute differently to insertion loss than to rms wavefront error. Specifically, we performed a multilinear least-squares fit of the loss data to a function of the form

$$IL = a_r w_{rms} + a_a w_{astig} + a_c w_{coma} + a_s w_{spherical} + a_0 \quad , \tag{4}$$

with five adjustable parameters a_r, a_a, a_c, a_s, and a_0. To isolate the dependence of loss on rms wavefront error from the components that specifically depend on the four aberration coefficients, we computed a linearly-corrected insertion loss defined by

$$IL_{corrected} = IL - a_a w_{astig} - a_c w_{coma} - a_s w_{spherical} - a_0 \quad . \tag{5}$$

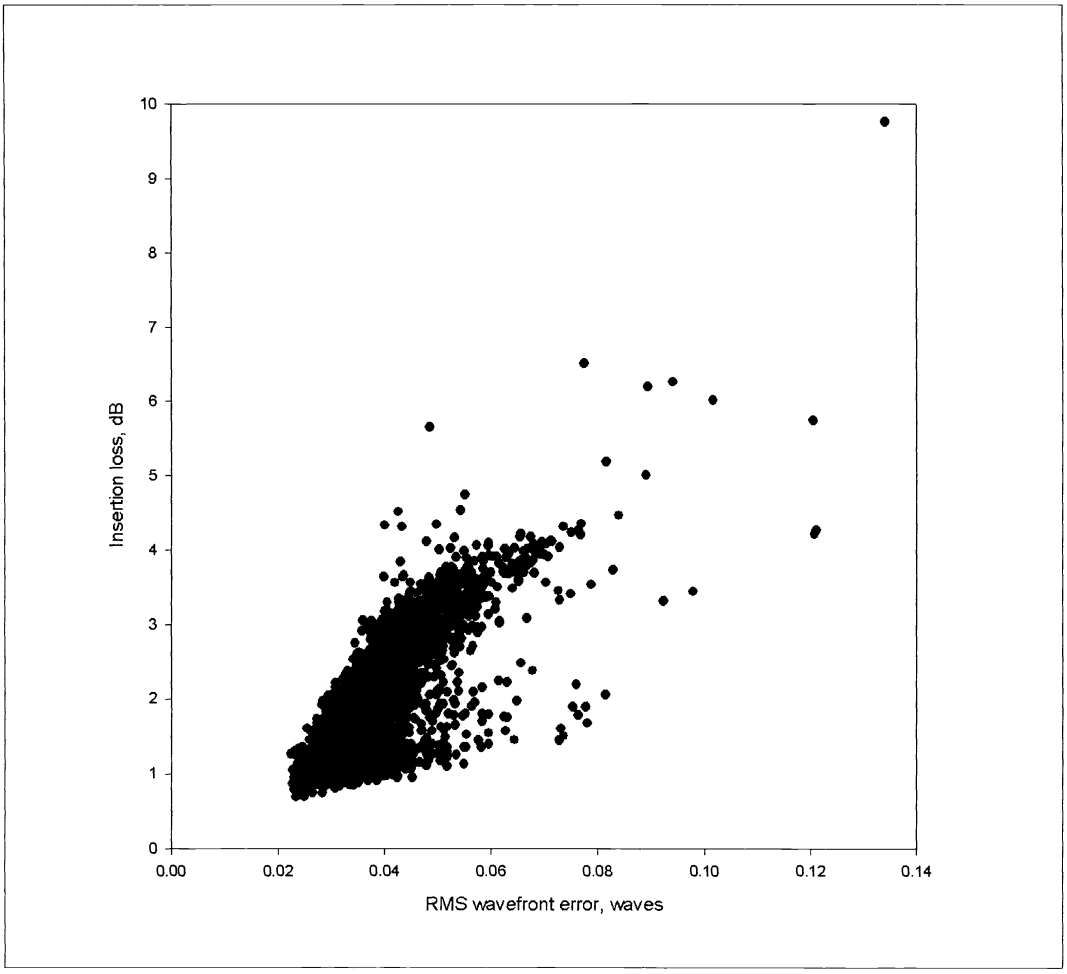

Figure 12: The raw double-pass insertion loss is plotted against the rms wavefront error measured by the interferometer.

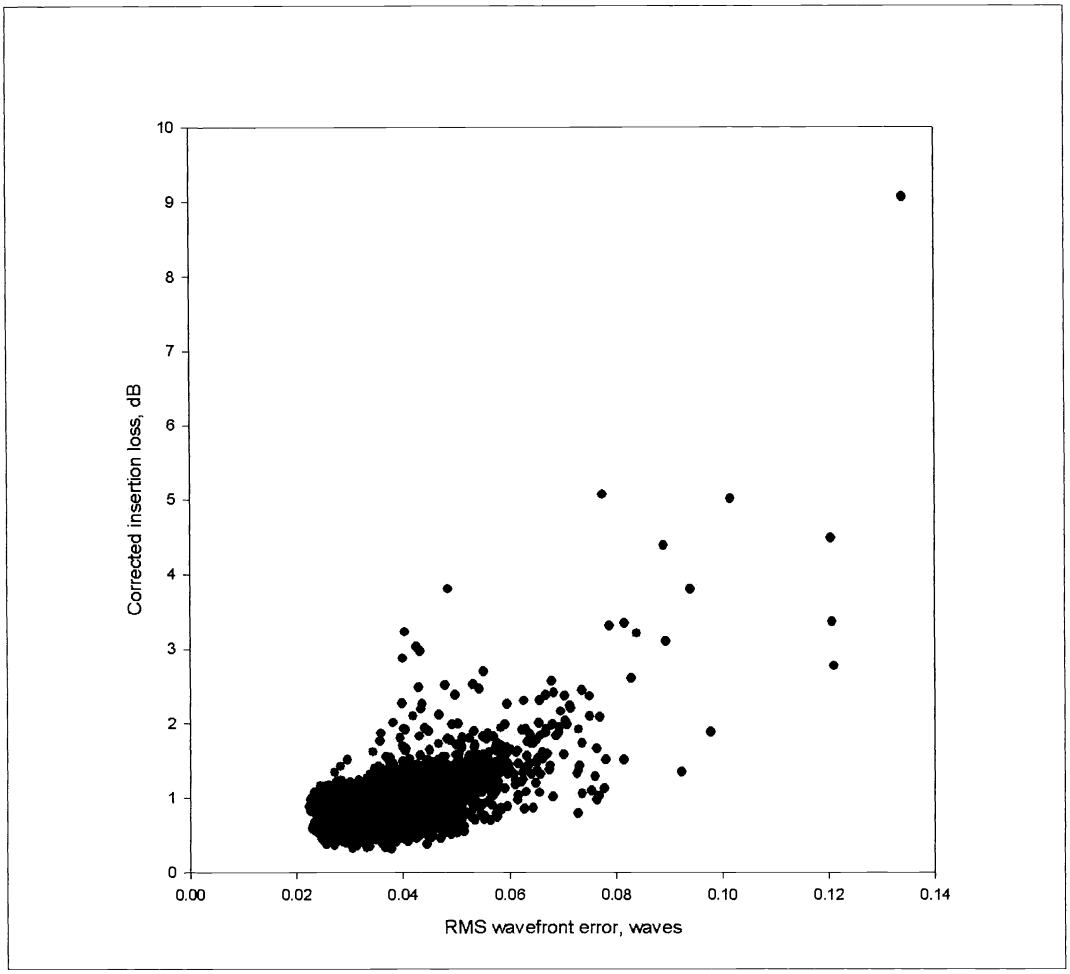

Figure 13: The linearly-corrected insertion loss, calculated by subtracting off the fitted linear dependences on astigmatism, coma, and spherical aberration, is plotted against the rms wavefront error. The rms deviation of the data from a parabolic fit is 0.25 dB.

Figure 13 shows the dependence of this linearly-corrected loss on wavefront error. The range of loss variation is now reduced considerably. The original multilinear fit to the data exhibits an rms error of 0.27 dB. A parabolic fit to the linearly-corrected data in Fig. 13 has even lower rms error: 0.25 dB. This error is adequate for our purposes and is the principal result of these measurements: the interferometeric measurements can predict the insertion loss to within 0.3 dB (rms).

There are many outlying data points in Fig. 13. These will be discussed in Section 4.1 below.

The same type of linear correction used to isolate the dependence of insertion loss on rms wavefront error can be performed to isolate its dependence on the other four measured parameters. Corrected in this way, the loss exhibits no dependence on astigmatism, as noted above, nor on coma (data not shown). These observations do not mean that astigmatism and coma do not contribute to insertion loss, because the measured parameters are not independent. Rather, these two aberrations contribute more weakly to loss than to rms wavefront error.

As shown in Fig. 14, the linearly-corrected insertion loss depends strongly on the coefficient of spherical aberration. The weak curvature in Figs. 12 and 13 led us to fit the loss data to a simpler function of the interferometrically-measured

parameters: a sum of parabolas in rms error and spherical aberration. The rms deviation of the data from this fit is further reduced to 0.24 dB.

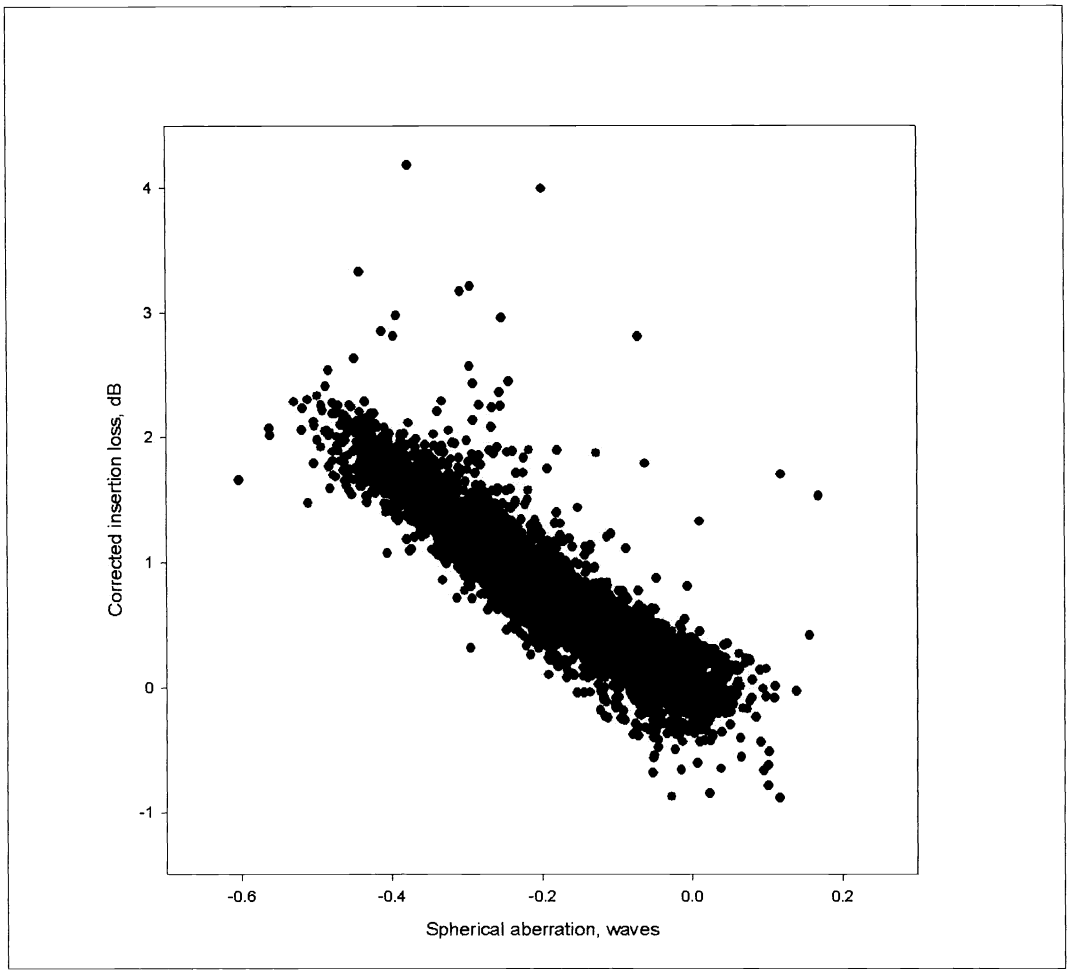

Figure 14: The linearly-corrected insertion loss (calculated by subtracting off the fitted linear dependencies on rms wavefront error, astigmatism, and coma) is plotted against the spherical aberration coefficient. A nearly linear dependence is observed.

4.1 Outliers and drop-outs

The fit of IL data exhibits numerous outliers. We examined the extreme outliers by hand to identify their cause. The outliers are mostly isolated high-loss lenses in the central, low-loss region of the lens array which appear to exhibit anomalously low aberrations. This observation raises a concern, since such aberration data would cause us to overlook high-loss lenses. However, these high losses did not reproduce during a second direct measurement; therefore, they represent false negatives. It should be pointed out that while both measurement techniques (direct and interferometric) may incorrectly identifying a high loss or aberration level; the opposite errors do not happen; i.e., a bad lens cannot accidentally be found to have low loss or low aberration.

Data drop-outs are also a potential problem in any scanning technique. In the present run, the interferometer was unable to acquire data for 8 of the 4356 lenses. These were found to be exclusively high-loss lenses; that is apparently why data acquisition was unsuccessful. This indicates that marking drop-outs as high loss is appropriate, because it is a conservative approach for rejecting a lens.

4.2 Next step – diffraction-based propagation model

A more general approach of relating wavefront error to IL is to construct a diffraction-based propagation model of the optical system shown in Figure 1a. The measured lens aberration would be incorporated into the model. IL would then be computed by numerical propagation of the beam through the optical system and into the fiber. This diffraction-based approach is required because the physical optics behavior is dominant and, as a result, geometrical-optics modeling is inadequate here. Diffraction-based models are currently being developed.

5. SUMMARY AND CONCLUSIONS

We have used a Twyman-Green interferometer to measure the BFL and transmitted wavefront error (and, indirectly, IL) of microlens arrays. Multiple measurements of BFL indicate that the measurement precision is 2 μm (1 standard deviation). It was also shown that paraxial Gaussian beam calculations qualitatively describe the dependence of IL on lens-to-fiber separation. Differences between theory and experiment are most likely due to residual aberrations in the lenses, which were not included in the model. Work is in progress to construct a diffraction-based model to include the effects of lens aberration.

Experimental results demonstrate that IL can be predicted from wavefront data to a precision of < 0.3 dB. The data for our lenses indicate that IL is strongly correlated to spherical aberration. Diffraction-based models are being developed to allow the IL to be computed directly from the measured transmitted wavefront error of the lens.

REFERENCES

1. Zygo Corporation, Laurel Brook Road, Middlefield, CT 06455-0448.
2. L. A. Selberg, "Radius measurement by interferometry," Opt. Eng. 31(9), 1961-1965 (1992).
3. M. V. Mantravadi, "Newton, Fizeau and Haidinger Interferometers", Chap 1 in *Optical Shop Testing, 2nd Edition*, D. Malacara, Ed., pp. 14 - 16, John Wiley & Sons, New York (1992).
4. OSLO Premium Edition, Ver. 6.1, Lambda Research Corporation, Littleton, MA 01460-4400.
5. R. E. Wagner and W. J. Tomlinson, "Coupling efficiency of optics in single-mode fiber components", Appl. Opt. 21(5), 2671-2688 (1982).